

## Facile Synthesis of BiOI Nanoparticles at Room Temperature and Evaluation of their Photoactivity Under Sunlight Irradiation

Vahid Mahmoodi<sup>1</sup>, Ali Ahmadpour<sup>1\*</sup> , Tahereh Rohani Bastami<sup>2</sup> and Mohammad Taghi Hamed Mousavian<sup>1</sup>

<sup>1</sup>Department of Chemical Engineering, Faculty of Engineering, Ferdowsi University of Mashhad, Mashhad, Iran

<sup>2</sup>Department of Chemical Engineering, Faculty of Engineering, Quchan University of Advanced Technology, Quchan, Iran

Received 28 April 2017, accepted 4 August 2017, DOI: 10.1111/php.12832

### ABSTRACT

In this study, highly photoactive BiOI nanoparticles (NPs) under sunlight irradiation were synthesized by a facile precipitation method using polyvinylpyrrolidone (PVP) at room temperature. The as-prepared catalysts were characterized by X-ray diffraction (XRD), scanning electron microscopy (SEM), transition electron microscopy (TEM), energy-dispersive X-ray spectroscopy (EDX), Fourier transform infrared (FTIR) and UV–vis diffuse reflectance spectra (UV–vis DRS). The results of XRD showed that PVP did not have any significant effect on tetragonal crystalline structure of BiOI. Also, using different amounts of PVP in the synthesis led to different morphologies and sizes of BiOI particles. It was found that using 0.2 g of PVP in the synthesis method changed morphology from 1- $\mu\text{m}$  platelets to NPs with size under 10 nm. In addition, the photocatalytic performance of prepared photocatalysts was evaluated in the photodegradation of reactive blue 19 (RB19) dye under sunlight irradiation. The BiOI synthesized using 0.2 g PVP (BiOI0.2) showed higher degradation efficiency compared to BiOI prepared without any additive. Excellent visible light photocatalytic properties of nano-scaled BiOI0.2 samples compared to BiOI platelets could be attributed to higher surface-to-volume ratio and narrow band-gap energy of as-prepared BiOI0.2 NPs.

### INTRODUCTION

Dye effluents are one of leading causes of environmental pollutions which are generated from a variety of sources such as paint and dye industries (1), textile units (2) and paper manufacturing (3). Due to their high organic content, dye effluents can cause different environmental problems in water resources. The presence of pollutants containing dyes in surface waters blocks light penetration through water, which creates negative effects on the aquatic ecosystem (4). On the other hand, dye effluents contain different types of synthetic dyes that are mainly toxic and exert carcinogenic and mutagenic effects on the creatures (5). Among different types of synthetic dyes, reactive dyes represent a class of high-colored materials that are extensively used in textile dyes (6). Anthraquinone-type reactive blue 19 (RB19) is one of the most common textile dyes with high resistance against chemical

degradation (7). The solubility of RB19 in water is relatively high (about 100 g L<sup>-1</sup>) (8). It has been shown that the chemical stability of RB19 is extremely high, and the estimated half-life of RB 19 at pH = 7.0 at 25°C was approximately 46 years (9).

Up to now, different techniques have been used for the removal of RB19 dye from wastewater including adsorption (10), biosorption (11), ultrafiltration (12) and nanofiltration (13). However, most of these methods are either time-consuming or transfer contaminants from one phase to another and therefore are unable to eliminate pollutions completely (14). Thus, it is necessary to find alternative techniques that are able to remove organic compounds from aqueous solution.

In recent years, semiconductor photocatalysis has provided a promising method for degradation of organic compounds such as polycyclic aromatic hydrocarbons (15), phenols (16), detergents (17), reactive dyes (18) and pharmaceutical compounds (19).

There are several in-depth studies on the mechanism of photocatalytic process (20). Generally, photocatalysis is a reaction which utilizes light to produce strong oxidative species and reactive holes with high reactivity tendency on a semiconductor surface to convert resistant organic materials into the inert components (e.g. CO<sub>2</sub>, H<sub>2</sub>O, phosphate, halide ions) (21). Titanium dioxide (TiO<sub>2</sub>) is one of the most important semiconductor photocatalysts due to its unique properties such as biological and chemical inactivity, high oxidative power, nontoxicity and high stability (14,21). However, TiO<sub>2</sub> is optically active in UV region ( $\lambda < 400$  nm) due to its limited optical properties (a band gap of 3.2 eV, fast recombination of electron–hole pair and so forth) (22). On the other hand, as the major light sources, sunlight is freely accessible and covers an extensive spectrum (200 nm  $< \lambda < 2400$  nm) (23). Actually, replacing UV or LED lamps with sunlight makes photocatalytic processes more economic. However, UV irradiation comprises only 3–5 percent of sunlight spectrum, and a significant proportion of sunlight is related to the visible light (43%) (24). Thus, for the application of sunlight irradiation, we need materials that could be optically active under visible light irradiation.

Bi oxides with a band gap ranging from 1.8 to 3.0 eV yield high photocatalytic efficiency under visible light irradiation (19). Among Bi oxides, bismuth oxyhalides (BiOX, X = Br, Cl, I) with its great electrochemical and optical properties have attracted growing attention in modern applications such as photocatalysis (25) and optoelectronic devices (26). Bi oxyhalides are characterized with a unique layered structure which makes them

\*Corresponding author email: ahmadpour@um.ac.ir (Ali Ahmadpour)  
© 2017 The American Society of Photobiology

the dominant family of photoactive materials under visible light irradiation. In fact, the electrical field between  $[\text{Bi}_2\text{O}_2]^{2+}$  sheets and  $\text{X}^-$  slabs inhibits electron-hole recombination which can increase the photocatalytic performance (27).

Bi oxyhalides are prepared by various processes such as hydrothermal/solvothermal techniques (28,29), hydrolysis (30), microwave-assisted technique (31) and wet chemical method (32). Zhang *et al.* reported a general one-pot solvothermal technique for the preparation of  $\text{BiOX}$  microspheres ( $\text{X} = \text{Br}, \text{Cl}, \text{I}$ ) using ethylene glycol as solvent (28). Further, photoactive  $\text{BiOBr}$  thin films have been successfully synthesized via a facile solvothermal reaction at different temperatures (29). Shi's group prepared  $\text{BiOCl}$  powders using a simple hydrolysis method which included the reaction between  $\text{BiCl}_3\text{-HCl}$  aqueous system and  $\text{Na}_2\text{CO}_3$  (30). Furthermore,  $\text{BiOCl}$  nanosheets unified in microflowers were synthesized using the microwave irradiation (31). Using a simple wet chemical route, Sharma's group synthesized  $\text{BiOX}$  ( $\text{X} = \text{Br}, \text{Cl}, \text{I}$ ) structures using five different solvent compositions prepared by mixing deionized water and ethanol. They found that the type and composition of the solvent played an important role in the structure and photocatalytic activity of the as-prepared structure (32).

Among  $\text{BiOX}$  catalysts, bismuth oxyiodide ( $\text{BiOI}$ ) has been the subject of growing attention due to its narrow band gap (1.7–1.8 eV), effective visible light activity and high degradation performance of organic compounds (33).

It is generally acknowledged that the size, shape and structure of heterogeneous catalysts dominate the optical, electrical and magnetic properties, among others, and directly control their catalytic performance (34). Motivated by this fact, many researchers have reported various morphologies of  $\text{BiOI}$  such as 3D microspheres (27,33), flower-like microspheres (35), hollow microspheres (36) and flake-like structures (32) all of which have shown relatively high photocatalytic performance in degradation of organic compounds under visible light irradiation.

On the other hand, it has been shown that nano-sized heterogeneous catalysts are more efficient at accelerating the catalytic processes compared to their bulk equivalents (37). Because of their higher surface-to-volume and larger number of active sites on catalyst surface, more catalytic reactions can be triggered at the same time. Moreover, nanoparticle catalysts are more conveniently dispersed in reaction mixture than do their bulk counterparts. Hence, it is anticipated that  $\text{BiOI}$  nanoparticles (NPs) exhibit enhanced photocatalytic performance compared to different  $\text{BiOIs}$  synthesized by other researchers. As far as authors are concerned, few studies have been carried out to prepare  $\text{BiOI}$  in form of nanoparticles.

In this study, first a facile precipitation method is presented for preparation of  $\text{BiOI}$  NPs (with size below 10 nm) at room temperature using a green solvent, ethanol and different amounts of polyvinylpyrrolidone (PVP). PVP is a water-soluble surfactant used as shape-controlling agent for synthesis of metallic nanostructures such as Ag nanoparticles (38–40), Ag nanowires (41), Co nanopowders (42), Pt nanoparticles (43) and Pd nanoparticles (44). In all of these nanostructures, PVP played two major roles: (1) stabilization of nanoparticles by hindering the agglomeration and (2) controlling growth via encapsulation of nanoparticles (39,42,44). So far, there is a paucity of studies on the synthesis of metal oxide nanoparticles by PVP.

Unlike other procedures, the synthesis method proposed in this study is very simple in terms of operation and only requires

a mixer and common solvents such as ethanol and water. The results showed that the size of  $\text{BiOI}$  NPs synthesized with 0.2 g of PVP ( $\text{BiOI0.2}$ ) was less than 10 nm. Enhanced photocatalytic activity of the as-prepared NPs was evaluated in the degradation of RB19 dye under sunlight irradiation. The  $\text{BiOI0.2}$  NPs exhibited more than 95% degradation efficiency for photodegradation of RB19 after 120 min of sunlight irradiation, while this value was 60% for the  $\text{BiOI}$  synthesized without PVP additive. Furthermore,  $\text{BiOI0.2}$  NPs showed great chemical and optical stability without any significant performance loss after four cycles. Thus, this work provided a simple method for large-scale production of  $\text{BiOI}$  NPs with high photocatalytic performance in degradation of different organic water contaminants under sunlight irradiation.

## MATERIALS AND METHODS

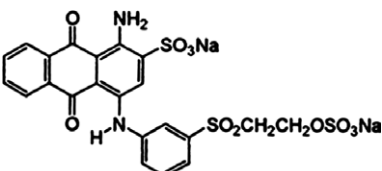
$\text{Bi}(\text{NO}_3)_3 \cdot 5\text{H}_2\text{O}$  (99%), as the Bi source, was purchased from Sigma-Aldrich. Also, potassium iodide (>99%) as I source, polyvinylpyrrolidone (PVP K25, molecular weight = 24000  $\text{g mol}^{-1}$ ), HCl (37% solution), NaOH, isopropyl alcohol (IPA), methyl alcohol and absolute ethanol were purchased from Merck. All chemicals were of analytical grade and were used as received without any further purification. Milli-Q water was used with a minimum resistivity of 18.2  $\text{M}\Omega \text{ cm}^{-1}$ . Reactive blue 19 (RB19) (with known properties as presented in Table 1) was purchased from Sigma-Aldrich.

**Synthesis of  $\text{BiOI}$  NPs.** The  $\text{BiOI}$  NPs were prepared using a facile precipitation method at room temperature. First, 0.34 g (0.7 mmol) of  $\text{Bi}(\text{NO}_3)_3 \cdot 5\text{H}_2\text{O}$  was stirred vigorously in 20 mL of ethanol for 60 min to obtain a homogenous white suspension. Then, certain amount of PVP (0.05 g, 0.1 g, 0.2 g) was added to the mixture, and stirring was resumed for a few minutes. Afterward, stoichiometric amount of KI (0.1162 g) was added to obtain a light yellow precipitate. After stirring for 12 h, the resulting orange precipitate was centrifuged and washed with absolute ethanol and deionized water several times. Finally, as-prepared  $\text{BiOI}$  samples were transferred to an oven and dried at 60°C overnight. For the sake of comparison,  $\text{BiOI}$  platelets were synthesized in a similar procedure with the exception of adding PVP. The samples synthesized with 0.05 g, 0.1 g and 0.2 g PVP were labeled as  $\text{BiOI0.05}$ ,  $\text{BiOI0.1}$  and  $\text{BiOI0.2}$ , respectively.

**Characterization.** The X-ray diffraction patterns were obtained by an X-ray diffractometer (XRD, D8-Advance Bruker) at room temperature using  $\text{Cu K}\alpha$  radiation ( $\lambda = 0.15406 \text{ nm}$ ) in a wide range of scanning angle ( $2\theta = 5\text{--}80^\circ$ ). The Fourier transform infrared (FTIR) of samples was recorded using Thermo Nicolet Avatar 370 FTIR in the range of 400–3900  $\text{cm}^{-1}$ . The size, shape and morphology of the prepared samples were analyzed by scanning electron microscopy (SEM, LEO 1450 VP) and transmission electron microscopy (TEM, LEO 912 AB). The UV–vis diffuse reflectance spectra (UV–vis DRS) of samples were obtained by a UV–VIS–NIR spectrophotometer (AvaSpec 2048 TEC) using  $\text{BaSO}_4$  as the reference standard.

To obtain the isoelectric point (IEP) of  $\text{BiOI0.2}$ , the zeta potential measurements were performed with a CAD instrument, ZetaCompact analyzer. In all experiments, the pH measurement was performed at room temperature using a HANNA pH meter (pH 211). UV–vis spectra and

**Table 1.** Physicochemical properties of reactive blue 19 (7).

Name	Chemical structure	Mw ( $\text{g mol}^{-1}$ )
Reactive Blue 19		626.5

concentration of RB19 dye were analyzed by a UV–vis spectrophotometer (Analyticjena, SPEKOL 1300). Also, total organic carbon (TOC) was measured by a TOC analyzer (TOC-V CSH, Shimadzu).

The possible photocatalytic degradation products of RB-19 were also detected by a gas chromatography/mass spectrometry (GC-MS) system (Thermoquest-Finnigan). The photodegraded samples were prepared for GC/MS analysis using the following method: First, samples were collected using a dichloromethane solvent (HPLC grade) in a separating funnel. Then, the samples were prepared under alkaline condition by adding 1 N sodium hydroxide (5 mL), followed by acidic extraction and addition of 1 + 1 concentrated sulfuric acid (5 mL) (45). Each extraction was conducted three times in 20 mL of dichloromethane. Then, anhydrous sodium sulfate was used for dehydration of extracts. Finally, extracted samples were concentrated to 10 mL using a rotary evaporator, and the concentration was continued to 100  $\mu\text{L}$  in n-hexane under  $\text{N}_2$  stream (46).

The GC system was equipped with a fused silica capillary DB-5 column (60 m  $\times$  0.25 mm i.d.; film thickness 0.25  $\mu\text{m}$ ) which was directly coupled to the MS system. The analysis conditions were as follows: the injection mode was set to splitless, while the injector temperature was equal to 250°C. The initial column temperature was kept constant for 2 min at 40°C and then increased to 100°C at a rate of 10°C  $\text{min}^{-1}$ . It was further ramped to 200°C at a rate of 10°C  $\text{min}^{-1}$  and raised to 270°C at 20°C  $\text{min}^{-1}$  and held constant for 5 min. Finally, the temperature was increased to 300°C at a rate of 10°C  $\text{min}^{-1}$  and retained constant for 5 min. Helium (99.99%) was used as the carrier gas at the flow rate of 0.8 mL  $\text{min}^{-1}$  (45,46). The products of RB19 photodegradation were identified by drawing a comparison between the GC–MS spectra patterns and those of Wiley Mass Spectral Library.

**Adsorption tests.** It should be noted that before performing the main photocatalytic experiments under the sunlight, a series of adsorption tests were carried out in the dark (Scheme 1). In all adsorption tests, 100 mL of dye solution (20 ppm, initial pH = 6.0) was prepared, and 0.05 g of as-prepared samples was immersed in the dye solution. Aliquots of the solution (about 3 mL) were sampled in the desired time intervals, and samples were centrifuged at 15455 g.

**Evaluation of photocatalytic activity.** The photocatalytic activity of the as-obtained samples was evaluated by the degradation of RB19 under sunlight irradiation. The photodegradation tests were performed in a 400-mL cylindrical Pyrex beaker. To ensure that illumination of the natural sunlight was sufficient, all photocatalytic tests were carried out between 10 am and 2 pm on sunny days in August 2016 at the city of Mashhad, Iran (GPS coordinates:  $N = 36.26^\circ$ ,  $E = 59.61^\circ$ ; Scheme 1). The ambient temperature was between 30°C and 32°C. As it was possible to vary the light intensity during the reaction, the intensity of the solar light was measured using a LT Lutron YK-2005LX digital light meter. The sensor was placed in a location that received the maximum intensity of solar light.

In a typical procedure, 0.05 g of the as-prepared photocatalyst was added to 100 mL of RB19 aqueous solution (20 ppm). If needed, the suspension pH was adjusted by HCl (0.1 M) and NaOH (0.1 M). Then, the suspension was magnetically stirred in the dark for 60 min to reach the adsorption–desorption equilibrium. Afterward, the beaker was subjected to the sunlight irradiation, and the suspension was sampled (3 mL)

at specified time intervals. All collected samples were immediately filtered and analyzed by measuring the absorption intensity at a maximum absorbance wavelength of  $\lambda = 600$  nm using UV–vis spectrophotometry with a 1-cm path length spectrometric quartz cell.

## RESULTS AND DISCUSSION

### Characterization of photocatalysts

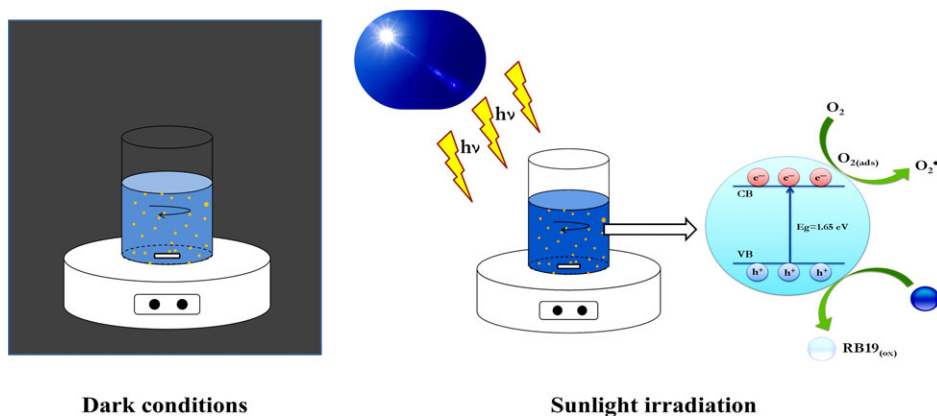
A schematic illustration has been presented for the possible process of BiOI NPs formation in the presence of PVP (Fig. 1). As n-polyvinylpyrrolidone has a dual hydrophobic–hydrophilic nature, it plays two major roles in the BiOI synthesis environment: (1) The hydrophobic portion of PVP acts as a stabilizer and protective agent and therefore inhibits the agglomeration of BiOI NPs (38,43). (2) PVP acts as a template for nucleuses and restrains the growing process by encapsulation of nanoparticles (42).

Thus, the formation process of BiOI NPs in the presence of PVP could be described as follows: As shown in Fig. 1, pentahydrate bismuth nitrate (III) is initially ionized and  $\text{Bi}^{3+}$  ions penetrate through PVP chains to coordinate with N or O atoms of PVP. In the next step, the adsorption of  $\text{I}^-$  anions within the PVP matrix produces initial nucleuses of BiOI. Finally, due to the restriction effect of PVP template, nucleuses grow in a controlled manner. In the presence of PVP, a similar mechanism was observed in the synthesis of cobalt nanopowders (42), Pt nanoparticles (43),  $\text{Ag}_4\text{SiW}_{12}\text{O}_{40}$  nanoparticles (47) and CdSe nanoparticles (48).

The crystal phase and purity of as-synthesized samples were evaluated by powder XRD analysis. The X-ray diffraction patterns of samples, BiOI, BiOI0.05, BiOI0.1 and BiOI0.2 are shown in Fig. 2.

All detectable peaks in these patterns can be indexed to the tetragonal phase of BiOI with space group  $P4/nmm$  (JCPDS Card No. 10-0445,  $a = 3.994$  Å,  $b = 3.994$  Å and  $c = 9.149$  Å). The fact that no other phases were detected from the possible impurity revealed high purity of samples. Some diffraction peaks of BiOI samples at  $2\theta$  values of 9.61°, 29.66°, 31.73°, 37.21°, 45.45°, 51.27°, 55.19°, 66.2° and 75.28° correspond to crystal planes of (001), (102), (110), (103), (104), (114), (212), (220) and (310), respectively (33,35,36).

The characteristic mean crystalline size of samples (d) was calculated using debye–scherrer’s equation, as follows (49):



**Scheme 1.** Experimental setup for the photocatalytic degradation of RB19 on as-prepared BiOI photocatalysts under dark and solar light conditions (volume of container = 400 mL).

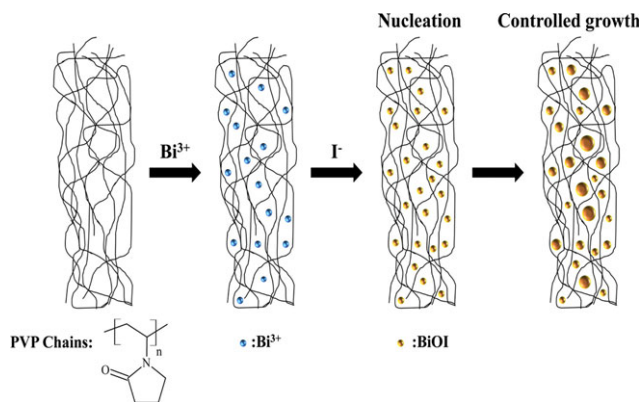


**Figure 1.** Schematic process for controlled formation of BiOI NPs using PVP additive.

$$d = \frac{K\lambda}{\beta \cos \theta} \quad (1)$$

where  $K$  is Scherrer constant ( $K = 0.94$ ),  $\lambda$  is the wavelength of X-ray ( $\lambda = 0.15406$  nm),  $\beta$  is the half-width of the diffraction peak and  $\theta$  is the Bragg's angle. The estimated mean crystallite size of BiOI, BiOI0.05, BiOI0.1 and BiOI0.2 was 19.38 nm, 10.03 nm, 7.62 nm and 7.38 nm, respectively.

The size, shape and morphology of BiOI samples were evaluated by SEM and TEM analysis, as shown in Fig. 3. According to Fig. 3a, when BiOI synthesis was carried out without adding any additive to the reaction system, BiOI platelets were obtained. However, the addition of PVP = 0.05 g did not have any significant effect on the morphology of BiOI platelets (Fig. 3b). Interestingly, with an increase in the amount of PVP, BiOI samples

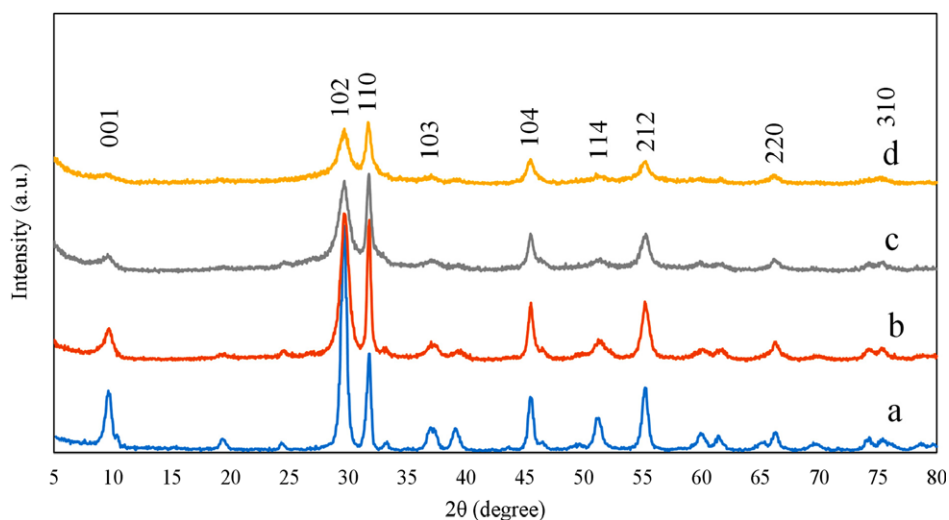


**Figure 2.** XRD patterns of as-prepared samples with different morphological structures, (a) BiOI, (b) BiOI0.05, (c) BiOI0.1 and (d) BiOI0.2.

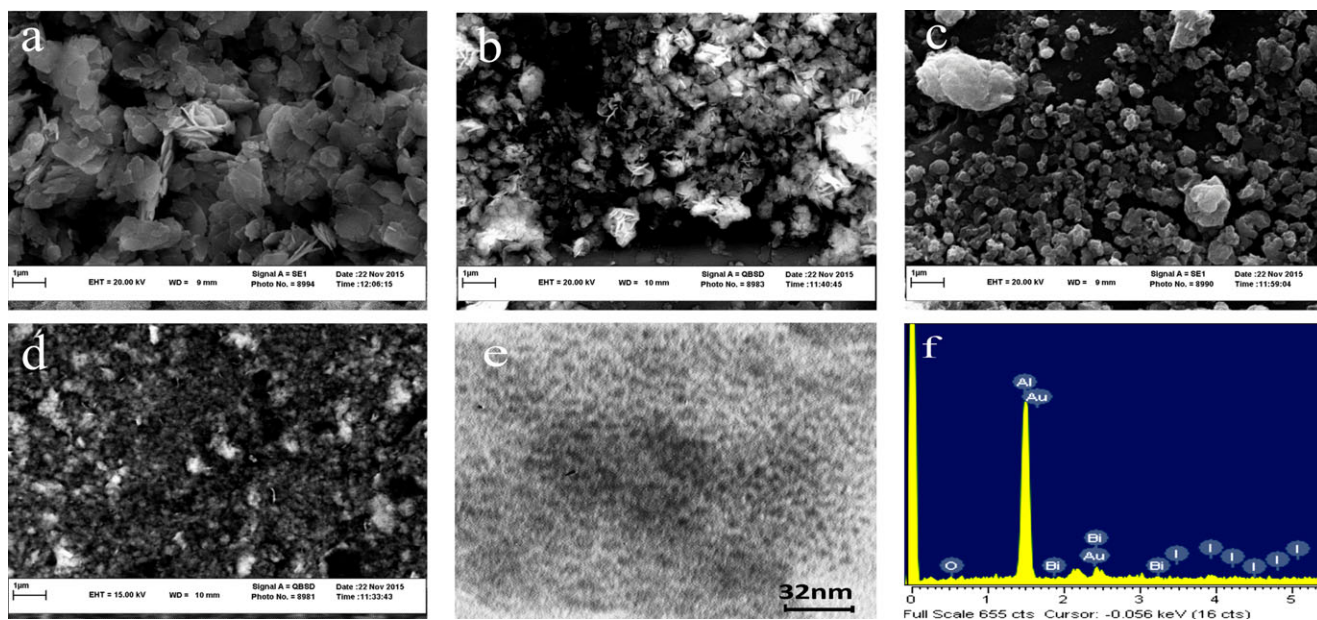


**Figure 3.** SEM images of (a) the BiOI platelets, (b) BiOI0.05, (c) BiOI0.1, (d) BiOI0.2, (scale bar = 1  $\mu$ m) (e) TEM image of BiOI0.2 (scale bar = 32 nm) and (f) EDS of BiOI0.2.

diminished in size, and the morphology of BiOI particles changed to spheroid particles (BiOI0.1) and nanoparticles (BiOI0.2), as shown in Fig. 3c and d. Moreover, BiOI NPs with a size less than 10 nm could be seen in Fig. 3e.

The BiOI0.2 samples were also analyzed by energy-dispersive X-ray spectroscopy. Figure 3f presents EDX analysis with characteristic X-ray lines of bismuth, iodide and oxygen. It is clear that small impurities of Au were appeared due to sample preparation steps. These results confirmed that PVP additives had an extraordinary effect on the morphology of BiOI.

FTIR spectra were used to study the surface chemistry of as-synthesized BiOI samples, as shown in Fig. 4. The peaks around 484, 480, 480 and 490  $\text{cm}^{-1}$  were related to the vibration of Bi=O=Bi bonds for BiOI, BiOI0.05, BiOI0.1 and BiOI0.2, respectively (50). The appearance of new adsorption band in the wave number (1290  $\text{cm}^{-1}$ ) in the FTIR spectrum of PVP can be attributed to the presence of C–N band, which is blueshifted to 1286, 1283 and 1282 for BiOI0.05, BiOI0.1 and BiOI0.2, respectively. This change could be ascribed to the interaction of nitrogen atom of PVP and BiOI samples (39,48). The multiple weak bands in the range of 1400–1500  $\text{cm}^{-1}$  are

related to the C=C stretching of aromatic pyridine groups and the vibration of tertiary nitrogen (38,48). In PVP spectrum, the observed band with high intensity at 1660  $\text{cm}^{-1}$  can be assigned to the stretching motion of carbonyl groups (40). In the case of BiOI samples synthesized with PVP, a blueshift to the lower wave numbers (almost 1650  $\text{cm}^{-1}$ ) was observed, which could be attributed to the interaction between the oxygen atom of PVP and BiOI NPs (40). Moreover, the broad peaks observed around 2954  $\text{cm}^{-1}$  and 3463 were due to the symmetric stretching vibrations of C–H bond and O–H stretching vibration of absorbed  $\text{H}_2\text{O}$  molecules, respectively (38,48). Generally, the results of FTIR spectra confirmed the interaction of PVP with BiOI NPs.

It is generally acknowledged that the energy band structure and optical properties of a semiconductor are directly related to its photocatalytic activity (51). Thus, the band-gap energy of as-synthesized samples was investigated using UV–vis diffuse reflectance spectra, as shown in Fig. 5a. The absorption spectra indicated that all fabricated BiOI samples were perfectly able to absorb the light in the UV and visible light region. Moreover, the absorption edges of samples were red-shifted with an

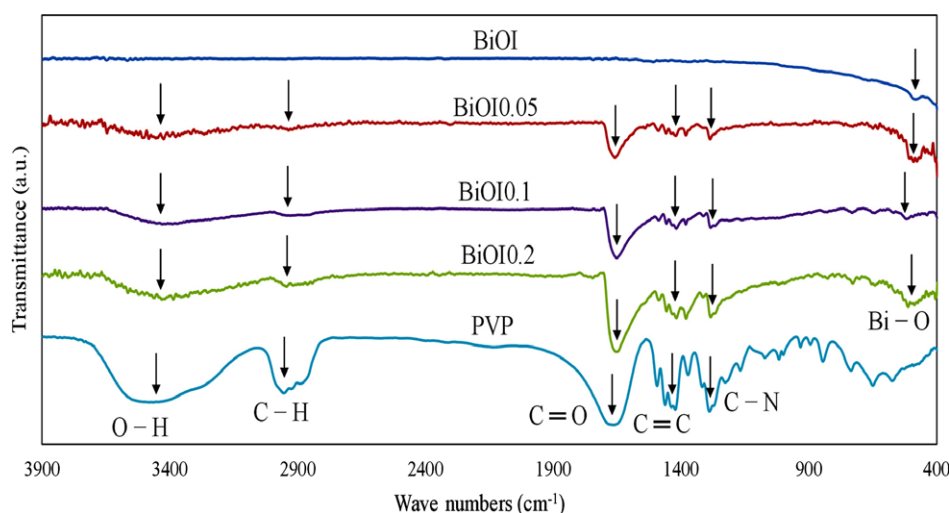


Figure 4. FTIR spectra of as-prepared samples.

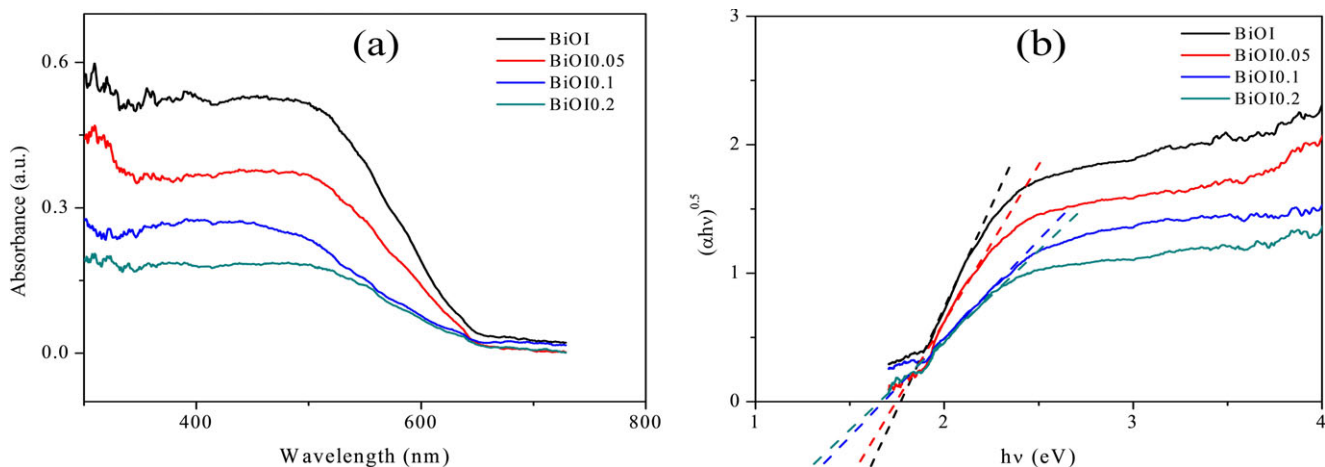
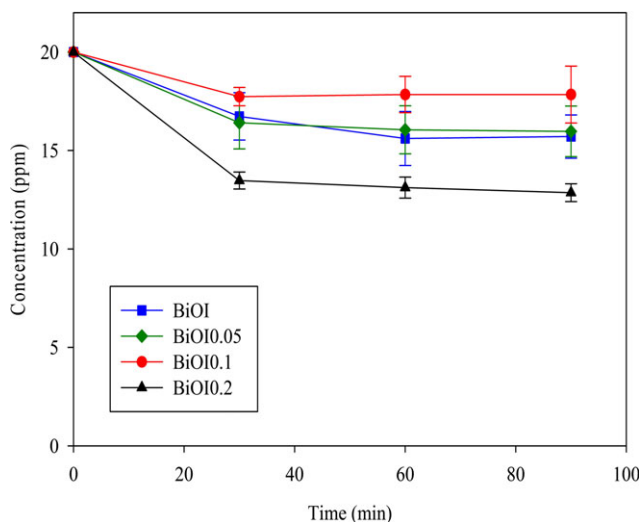
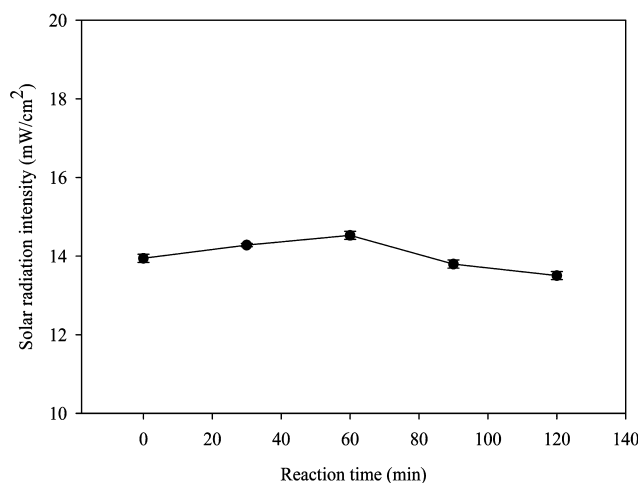


Figure 5. UV–vis spectra (a) and plots of the  $(\alpha hv)^{1/2}$  versus photon energy (b) for the as-synthesized BiOI samples.



**Figure 6.** Evaluation of RB19 dye adsorption on the surface of as-prepared BiOI samples in the dark.



**Figure 7.** Sunlight irradiation intensity versus photocatalytic reaction time.

increase in PVP. The band-gap energy of as-prepared BiOI samples can be calculated by the following equation (50):

$$\alpha h\nu = A(h\nu - E_g)^{n/2} \quad (2)$$

where  $\alpha$ ,  $h$ ,  $\nu$ ,  $A$  and  $E_g$  represent the adsorption coefficient, Planck constant, incident light frequency, a constant and band-gap energy, respectively. In addition,  $n$  depends upon characteristics of the optical transition of semiconductor ( $n = 1$  for a direct transition and  $n = 4$  for an indirect transition). In the case of indirect transition of BiOI, we have  $n = 4$  (50). Thus, the corresponding values of the indirect band gap of samples could be estimated by drawing the plot of  $(\alpha h\nu)^{1/2}$  versus photon energy ( $h\nu$ ), as shown in Fig. 5b. The intercept of the tangent to the  $X$ -axis would give a good approximation of the band-gap energy of samples. The estimated band gaps of BiOI, BiOI0.05, BiOI0.1 and BiOI0.2 were 1.77, 1.74, 1.68 and 1.65 eV, respectively.

It is well known that in semiconductors, by decreasing particle size, band gap increases due to the quantum confinement effect (52). But in the case of nanoparticles embedded in a matrix, some other factors may affect the band gap such as surrounding

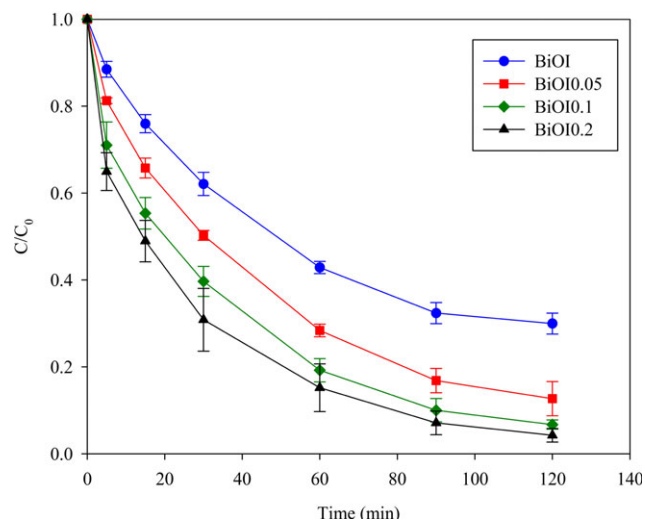


**Figure 8.** The photocatalytic activity of as-prepared BiOI samples on the degradation of RB19 dye under natural sunlight irradiation. [Color figure can be viewed at [wileyonlinelibrary.com](http://wileyonlinelibrary.com)]

matrix effect, surface and interface condition, surface pressure and lattice strain (52,53).

Deotale and Nandedkar claimed that the band gap of very small nanoparticles is affected by the pressure surface effect, so that for very small size nanoparticles, surface pressure and lattice strain increase leading to band-gap reduction (53). Also, Nanda *et al.* reported that in the case of semiconductor nanoparticles embedded in a matrix, the surface and interface effects of surrounding matrix may influence the value of band gap (52). So in this research, decreasing the band gap of extremely small BiOI0.2 NPs could be attributed to increasing the surface pressure. Actually, by increasing the surface pressure of BiOI0.2 NPs, the lattice strain in the sample increases leading to reduction in BiOI0.2 NPs band gap (53). Also, the interface effects of PVP matrix and surface conditions of the sample may counteract the influence of quantum confinement (52). For more detailed discussion, interested readers are referred to Nair *et al.* (54) and Kumar *et al.* (55).

The lower band-gap energy of BiOI0.1 and BiOI0.2 confirmed that these samples could be excited easily and generate more electron-hole pairs on the surface. This leads to higher photocatalytic performance for degradation of organic pollutants under sunlight irradiation. These results indicated that the energy band structure and optical properties of BiOI were obviously affected by amount of PVP in the synthesis process.

### Photocatalytic activity

Figure 6 shows the results of adsorption experiments in the dark. It was found that the adsorption-desorption equilibrium was achieved after 60 min, and in photocatalytic experiments, the concentration of RB19 at this time was considered as the initial concentration ( $C_0$ ).

To consider the variability of the sunlight irradiation, the light intensity was measured during the photocatalytic reaction, and the results are shown in Fig. 7. It was found that during the reaction, sunlight irradiation intensity did not change significantly and varied in the range of 13.5–14.5  $\text{mW cm}^{-2}$ , approximately.

To evaluate the photocatalytic activity of the as-prepared samples, the degradation of RB19 dye in an aqueous solution was measured under sunlight. The results are presented in Fig. 8. As

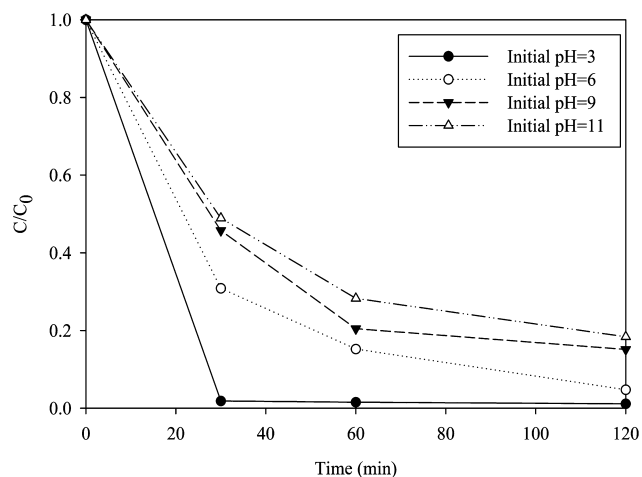


**Figure 9.** The effect of initial pH of RB19 solution on photocatalytic performance of BiOI0.2 NPs.

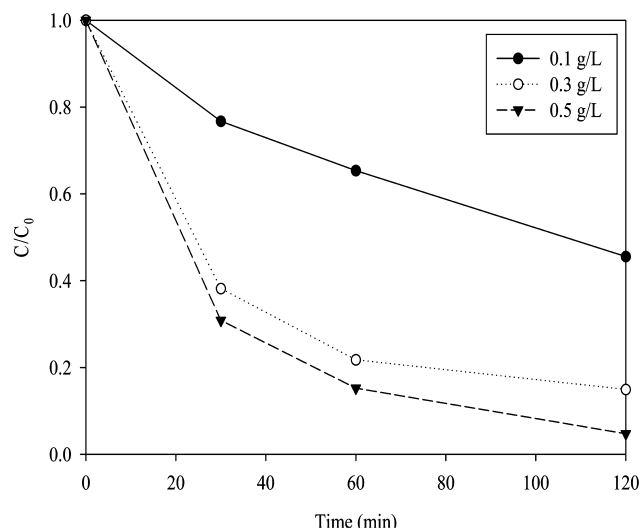


**Figure 10.** The effect of BiOI0.2 dosage on photocatalytic degradation of RB19.

can be seen in the case of BiOI platelets, the degradation efficiency of RB19 was about 65% within 120 min, whereas for BiOI0.2 NPs, the degradation efficiency increased up to 95%. Moreover, the results of TOC analysis showed that the

corresponding TOC for initial RB19 (20 ppm) was  $13.12 \text{ mg L}^{-1}$ , while for BiOI0.2, it was reduced to  $7.588 \text{ mg L}^{-1}$  after 120 min sunlight irradiation.

There are several reasons for the increased photoactivity of the BiOI0.2 NPs over BiOI platelets. First, it has been shown that nano-sized catalysts exhibit higher surface-to-volume ratio compared with bulk type, and therefore, BiOI0.2 NPs provide more active sites for photocatalytic reaction. As well, enhanced dispersion leads to higher light absorption efficiency (56). It is helpful to provide more photoexcited electrons and holes as reactive species and enhance the photocatalytic degradation of contaminants (50). The second reason is the narrow band gap of BiOI0.2 (1.65 eV), as observed in the UV-vis DRS results. Therefore, under the sunlight irradiation, larger number of photoexcited electron-hole pairs would be generated on the surface of BiOI0.2 samples. Thus, excellent visible photocatalytic properties of nano-scaled BiOI0.2 samples could be attributed to a larger surface-to-volume ratio, higher light absorption capacity and narrow band-gap energy of as-prepared BiOI0.2 NPs.

It has been proved that the initial pH of the solution is a key parameter in the photocatalytic degradation of organic compounds (57,58). So, the effect of initial pH of dye solution on photocatalytic performance was investigated at different pH values (3,6,9,11), and the corresponding results are shown in Fig. 9. It should be mentioned that the initial pH of RB19 solution was about 6 which was in agreement with reported values in the literature (59). Also, it has been demonstrated that at the pH ranging from 3 to 10, RB19 shows great stability against pH and has a net negative charge at this pH range (59).

As shown in Fig. 9, it was found that the degradation performance of RB19 was extremely increased at lower pH values (pH = 3). On the other hand, the results of zeta potential measurements proved the IEP of BiOI0.2 is about 2.92, as presented in Figure S1. This value was completely matched with the results of other researchers in the literature (60). It suggests that at pH 2.92, the average surface charge of BiOI0.2 will be close to zero. Also, the surface of BiOI0.2 is positively charged below pH 2.9 and negatively charged above IEP. Therefore, the higher photocatalytic performance of BiOI0.2 at lower pH values could be attributed to the better adsorption of RB19 on the surface of BiOI0.2 due to the lack of electrostatic repulsion between RB19 molecules and BiOI0.2 surface. Also, it is suggested that other interactions such as van der Waals forces and hydrogen bonding between RB19 molecules and carbonyl groups of BiOI0.2 surface are more effective. Conversely, at pH values higher than

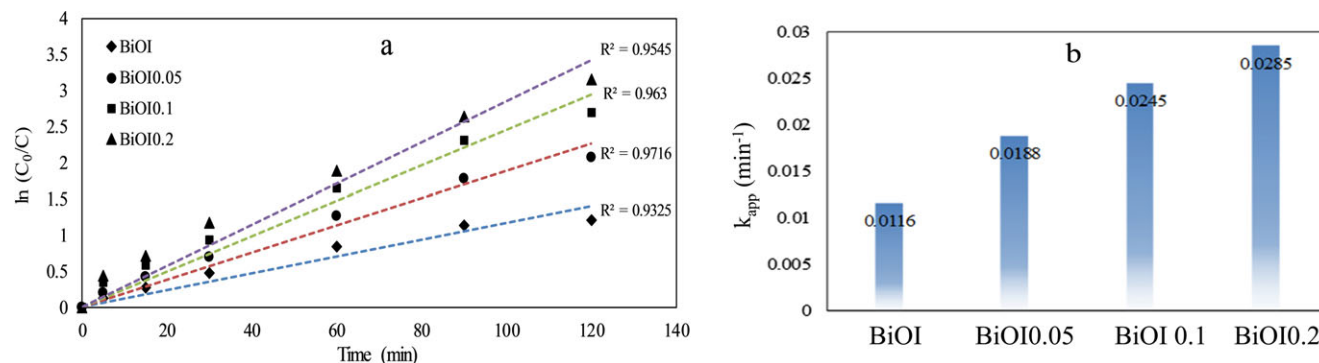


**Figure 11.** The kinetic plots (a) and pseudo-first-order constants (b) of photocatalytic degradation of RB19 under the sunlight irradiation. [Color figure can be viewed at [wileyonlinelibrary.com](http://wileyonlinelibrary.com)]

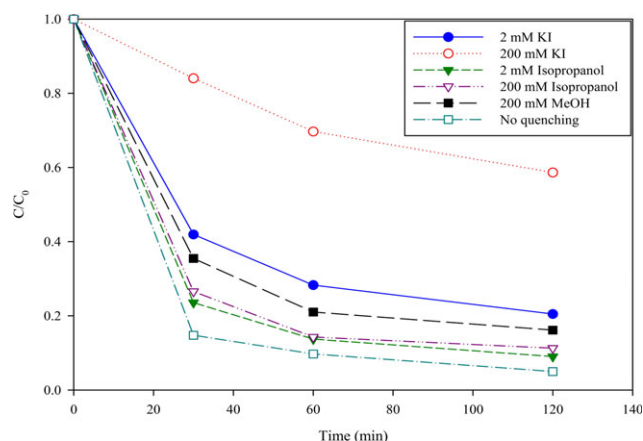
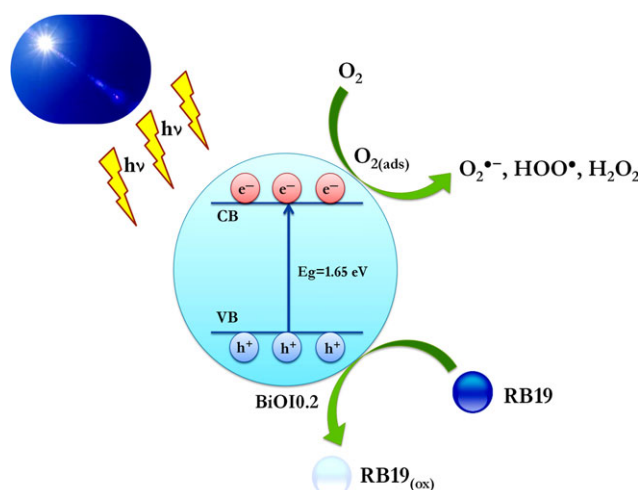


**Figure 12.** Trapping experiments of photodegradation of RB19 with the presence of different scavengers under the sunlight irradiation.



**Scheme 2.** Schematic diagram of the photocatalytic reaction of RB19 on BiOI nanoparticles.

IEP of BiOI, the surface of BiOI is negatively charged, and high repulsive forces between BiOI and negative-charged molecules of RB19 led to decreased adsorption of dye molecules on the surface of photocatalyst and photocatalytic performance reduction, consequently. Furthermore, the higher photocatalytic efficiency at neutral and acidic pH range could be attributed to the deactivation of photogenerated holes on the surface of BiOI NPs at alkaline pH values, according to the following reaction (61):



Actually, above IEP of BiOI NPs, the photocatalyst surface is negatively charged by adsorption of hydroxide anions. The presence of large number of  $\text{OH}^-$  ions on the photocatalyst surface leads to deactivation of the photogenerated holes and formation of hydroxyl radicals in the reaction medium, according to Eq. 3 (61,62). It should be noted that in the present research, hydroxyl radicals have no significant role in the photocatalytic degradation of RB19, and photogenerated holes are the main causes of photocatalytic reaction. (It will be proved later in the trapping experiments section.) Therefore, at alkaline pH,

**Table 2.** Possible products of RB19 photodegradation identified by GC-MS analysis.

Product	Chemical structure	Chemical formula	$M_w$
Indoline		$\text{C}_8\text{H}_9\text{N}$	119.2
Coumarin		$\text{C}_9\text{H}_6\text{O}_2$	146.1
3-Carboxytyrosine		$\text{C}_{10}\text{H}_{11}\text{NO}_5$	225.2
2-[(3-Oxo-1,3-dihydro-2-1, benzofuran-1-yl) 1,methyl] benzoic acid		$\text{C}_{16}\text{H}_{12}\text{O}_4$	268.3
Dihydroxanthin		$\text{C}_{17}\text{H}_{24}\text{O}_5$	308.4
Desulphosinigrin		$\text{C}_{10}\text{H}_{17}\text{NO}_6\text{S}$	279.3
Cystathionine		$\text{C}_7\text{H}_{14}\text{N}_2\text{O}_4\text{S}$	222.3

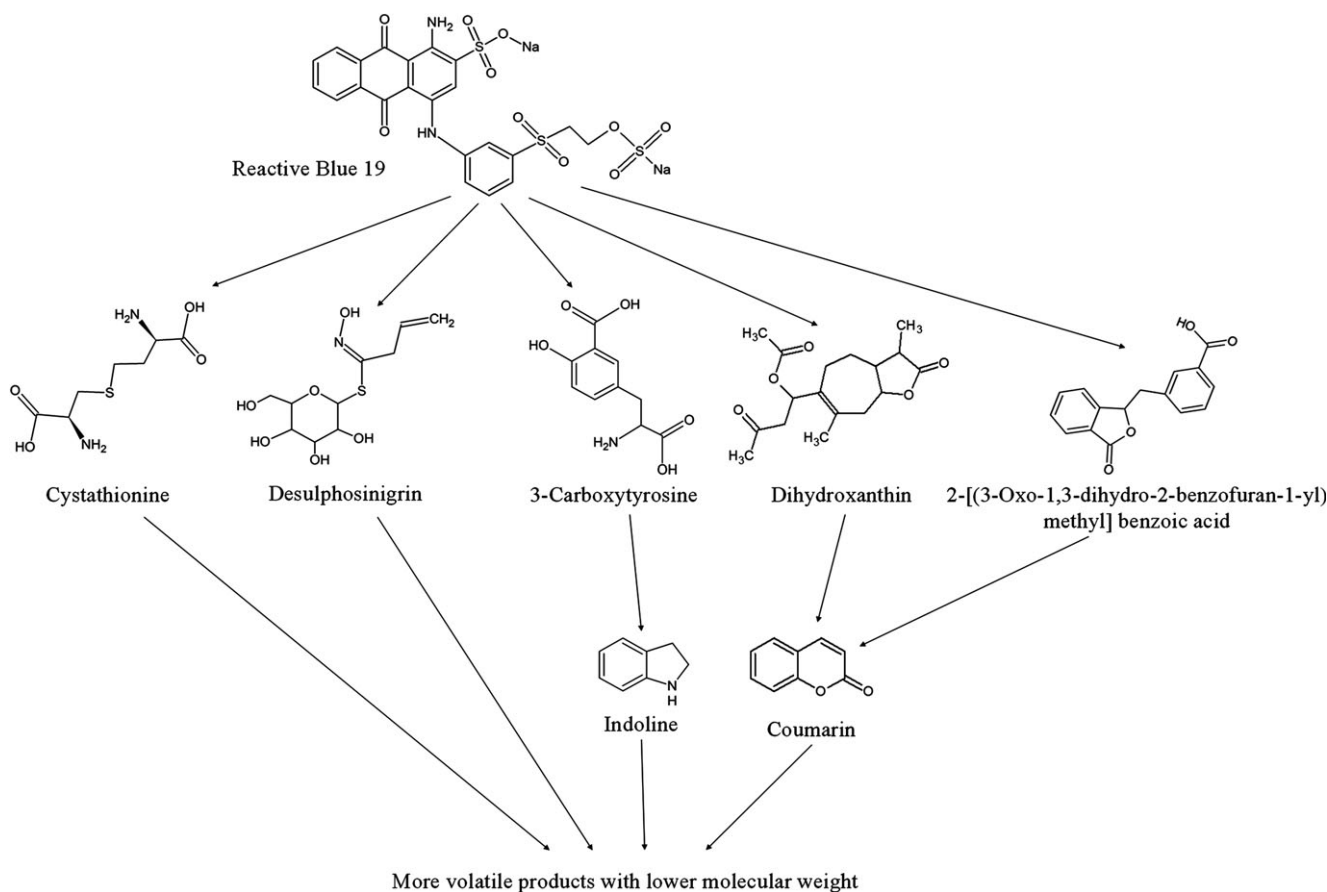


**Figure 13.** Proposed mechanism for photocatalytic degradation of RB19 under the sunlight irradiation.

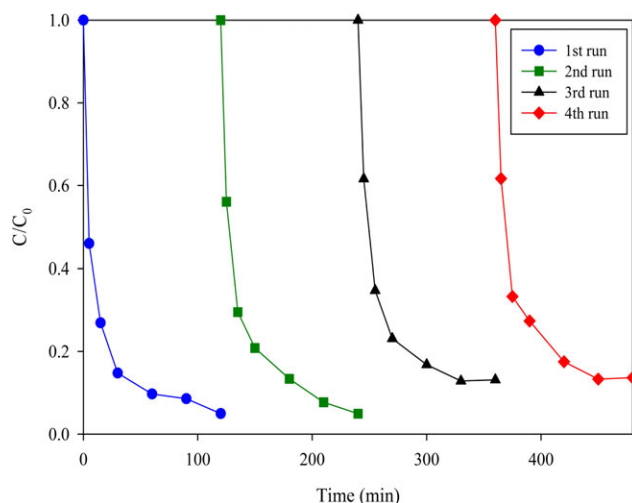


**Figure 14.** Recycle experiments of BiOI0.2 NPs for photocatalytic degradation of RB19 under sunlight irradiation. [Color figure can be viewed at [wileyonlinelibrary.com](http://wileyonlinelibrary.com)]

photogenerated holes are deactivated, and production efficiency of hydroxyl radical increases leading to reduction in photocatalytic efficiency.

Also, the influence of BiOI0.2 dosage on the photocatalytic degradation of RB19 was investigated at three different BiOI0.2 concentrations (0.1, 0.3 and 0.5 g L<sup>-1</sup>), and the corresponding

results are shown in Fig. 10. It was clearly observed that at lower BiOI0.2 concentrations, the photocatalytic degradation efficiency was low, and  $C/C_0$  reached to 0.46 and 0.15 for concentrations of 0.1 and 0.3 g L<sup>-1</sup>, respectively. But, when the photocatalyst dosage increased up to 0.5 g L<sup>-1</sup>,  $C/C_0$  was greatly decreased to 0.04. This result could be explained by different terms such as the active sites on BiOI0.2 surface and the light absorption capacity (58). Actually, higher photocatalyst dosage provides more active BiOI0.2 surface sites for photocatalytic reaction. Moreover, increasing the amount of BiOI0.2 photocatalyst leads to the higher light absorption capacity and increased photocatalytic performance.

To study the kinetics of degradation of RB19 dye, the Langmuir–Hinshelwood (L-H) model was evaluated with the measured concentrations of RB19. It is generally accepted that L-H model is the most widely used mechanism to clarify the kinetics of heterogeneous photocatalytic systems (63). For low liquid-phase concentrations of the organic pollutant, simplified L-H model is used where  $k_{app}$  represents the pseudo-first-order reaction rate constant and  $C_0$  is the initial concentration of the pollutant (15):

$$\ln\left(\frac{C}{C_0}\right) = -k_{app}t \quad (4)$$

It is noteworthy that Eq. (4) is applicable at low concentrations of substrate, and compared to water, the initial concentration of RB19 is negligible. The simplified L-H model (Eq. 4)

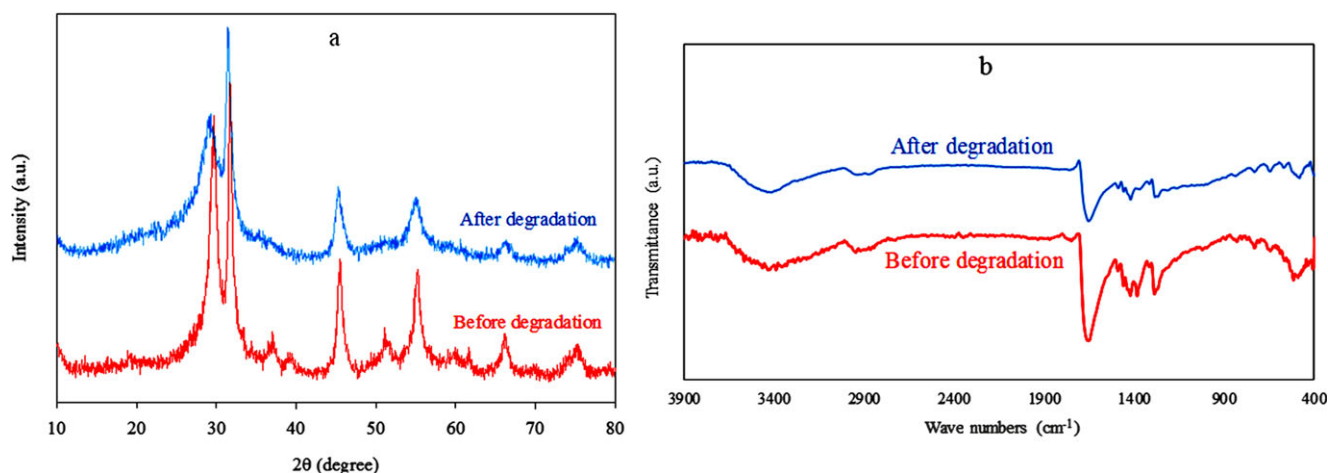


**Figure 15.** (a) XRD pattern and (b) FTIR spectrum of recycled BiOI<sub>0.2</sub> NPs before and after photocatalytic degradation of RB19.

was used to describe the kinetics of photocatalytic degradation of RB19, and the experimental results showed good agreement with the model (Fig. 11a).

Moreover, as shown in Fig. 11b, the estimated pseudo-first-order reaction rate constants were 0.0116, 0.0188 and 0.0245 min<sup>-1</sup> for BiOI, BiOI<sub>0.05</sub> and BiOI<sub>0.1</sub>, respectively. The removal efficiency of BiOI<sub>0.2</sub> was much higher than other samples, and the  $k_{app}$  was 0.0285 min<sup>-1</sup>, which was twice higher than that of BiOI.

#### Trapping experiments and proposed mechanism for photodegradation of RB19

To clarify the photocatalytic mechanism of BiOI NPs, main active species in the photocatalytic degradation should be determined using trapping experiments of oxidative agents such as hydroxyl and superoxide radicals ( $\text{OH}^\bullet$ ,  $\text{O}_2^{\bullet-}$ ) and holes ( $\text{h}^+$ ). It was performed using KI ( $\text{OH}^\bullet$  and  $\text{h}^+$  scavenger), Isopropyl alcohol (IPA) ( $\text{OH}^\bullet$  scavenger) at two concentrations (2 mM and 200 mM) and methyl alcohol (MeOH) ( $\text{O}_2^{\bullet-}$  scavenger) at 200 mM (22). Also, under the same conditions, control tests were performed in the absence of any quenching agents. The results of RB19 degradation efficiency over BiOI<sub>0.2</sub> NPs are presented in Fig. 12.

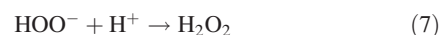
The addition of 2 mM IPA to RB19 solution did not have any significant effect on photodegradation efficiency of RB19. Also, increasing IPA concentration up to 200 mM did not cause a significant change in photodegradation activity. Thus, it was concluded that  $\text{OH}^\bullet$  radicals on the surface of BiOI did not play a major role in the photocatalytic reaction. On the other hand, the addition of 2 mM KI led to a moderate decline in photocatalytic performance, while 200 mM KI reduced the photodegradation efficiency more than 60%. As such, it was evident that photoexcited holes on the surface of photocatalysts played a major role in the photocatalytic degradation of RB19.

Moreover, it was observed that MeOH exerted a slight effect on photocatalytic system, suggesting that the superoxide radicals ( $\text{O}_2^{\bullet-}$ ) acted as assistants in photocatalytic degradation of RB19 under the sunlight irradiation.

Based on the above results, a schematic diagram was presented for photocatalytic reaction of RB19 on BiOI<sub>0.2</sub> NPs, as shown in Scheme 2. BiOI<sub>0.2</sub> NPs were activated under the sunlight irradiation, and electrons were excited from the valence band (VB) to the conduction band (CB). After the generation of

electron-hole ( $\text{e}^-$ - $\text{h}^+$ ) pairs, adsorbed RB19 molecules were immediately oxidized by  $\text{h}^+$  on the surface of BiOI<sub>0.2</sub> NPs (direct oxidation). On the other hand, the combination of oxygen adsorbed on the surface of BiOI with photoexcited electron led to the formation of superoxide radicals ( $\text{O}_2^{\bullet-}$ ). It could inhibit the recombination of photoexcited electron-hole pairs and provided adequate charge separation and effective photocatalytic degradation.

Moreover, the generated superoxide radicals were able to form hydroperoxyl radicals ( $\text{HOO}^\bullet$ ) and subsequently  $\text{H}_2\text{O}_2$  by equations as follows (20):



#### Photodegradation products and possible degradation pathway of RB19

To identify the products of photocatalytic RB19 degradation under sunlight irradiation, GC/MS analysis was performed. The possible products are listed in Table 2. The results showed the formation of some volatile compounds with lower molecular weight such as indoline, coumarin, 3-carboxytyrosine, 2-[(3-oxo-1,3-dihydro-2-benzofuran-1-yl) methyl] benzoic acid, dihydroxanthin, desulphosinigrin and cystathionine. It was clear that photocatalytic reaction on the surface of BiOI<sub>0.2</sub> NPs had led to cleavage of anthraquinone rings and degradation of RB19. GC-MS chromatogram of photodegraded sample and possible intermediates are given in Figure S2.

Based on the results of GC/MS analysis, a possible mechanism was proposed for photodegradation of RB19, as shown in Fig. 13.

The mechanism suggested that photocatalytic reaction could lead to the complete destruction of anthraquinone rings, which produced compounds such as cystathionine or desulphosinigrin. However, partial degradation of anthraquinone rings could generate compounds such as dihydroxanthin, 3-carboxytyrosine and 2-[(3-oxo-1,3-dihydro-2-benzofuran-1-yl) methyl] benzoic acid.

These components could be then converted into lighter and more volatile compounds such as coumarin and indoline. Finally, all these compounds might be degraded to compounds with much lower molecular weight such as CO<sub>2</sub>, H<sub>2</sub>O and phosphate (20).

### Stability and reusability

The consecutive recycle runs were performed to investigate the reusability and optical stability of BiOI0.2 NPs without any recovery process. As shown in Fig. 14, no significant loss was observed in photocatalytic performance, and the degradation efficiency was about 85% in the fourth cycle. According to the results, there was no significant photocorrosion on the surface of BiOI0.2 NPs during photocatalytic degradation of RB19.

Moreover, the XRD pattern and FTIR spectra of the recycled BiOI0.2 NPs were investigated, as shown in Fig. 15(a) and (b). As can be seen, there was no significant change in the position and intensity of XRD diffraction peaks and FTIR spectrum of recycled BiOI0.2 NPs. These results suggested excellent chemical stability of BiOI0.2 NPs, which could be used several times for photocatalytic degradation of model pollutant compounds under sunlight irradiation.

### CONCLUSIONS

In this study, we presented a PVP-assisted one-pot method for preparation of BiOI NPs at room temperature. The as-synthesized samples were characterized by several techniques such as X-ray diffraction (XRD), scanning electron microscopy (SEM), transmission electron microscopy (TEM), energy-dispersive X-ray spectroscopy (EDX), Fourier transform infrared (FTIR) and UV–vis diffuse reflectance spectroscopy (UV–vis DRS). To evaluate the photocatalytic activity of the as-prepared samples, the degradation of reactive blue 19 dye in an aqueous solution was examined under sunlight irradiation. It was found that PVP amount in the BiOI synthesis method played an important role in the morphological structure and photocatalytic properties. The size of BiOI synthesized with 0.2 g of PVP was smaller than 10 nm, and it showed maximum photocatalytic efficiency owing to higher surface-to-volume ratio, superior dispersion ability and narrow band-gap energy. The effect of some operational parameters such as initial pH of solution and photocatalyst dosage was examined on photocatalytic degradation of RB19. The results showed that higher photocatalytic performance was achieved at acidic pH range and high concentration of BiOI0.2 NPs. To investigate the photocatalytic mechanism of BiOI0.2 NPs, a series of trapping experiments were conducted with/without the presence of radical scavengers. The results showed that photoexcited holes on the surface of photocatalysts played a key role in the photocatalytic degradation of RB19. Also, to clarify the photocatalytic degradation pathway of RB19 under sunlight irradiation, the possible intermediates were identified using gas chromatography coupled with mass spectroscopy (GC/MS), and a photodegradation mechanism was proposed. Furthermore, the as-prepared BiOI0.2 NPs exhibited excellent reusability and photocatalytic stability after four recycles. In conclusion, this work suggests that synthesized BiOI0.2 NPs were favorable photocatalyst for the degradation of model pollutant compounds under

sunlight irradiation. Further, the synthesis method could be utilized for synthesis of other Bi oxides with unique properties.

*Acknowledgements*—The support of Ferdowsi University of Mashhad (Research grant) is appreciated for this work. This research has also been supported by the “Iran Nanotechnology Initiative Council.”

### SUPPORTING INFORMATION

Additional Supporting Information may be found in the online version of this article:

**Figure S1.** The effect of pH on zeta potential of BiOI0.2 NPs.

**Figure S2.** GC–MS chromatograms of (a) photodegraded sample and possible products, (b) Indoline, (c) Coumarin, (d) 3-Carboxytyrosine, Dihydroxanthin and 2-[(3-Oxo-1,3-dihydro-2-benzofuran-1-yl) methyl] benzoic acid, (e) Desulphosinigrin, (f) Cystathionine.

### REFERENCES

- Rao, V. B. and S. R. M. Rao (2006) Adsorption studies on treatment of textile dyeing industrial effluent by flyash. *Chem. Eng. J.* **116**, 77–84.
- Abidi, N., E. Errais, J. Duplay, A. Berez, A. Jrad, G. Schäfer, M. Ghazi, K. Semhi and M. Trabelsi-Ayadi (2015) Treatment of dye-containing effluent by natural clay. *J. Clean. Prod.* **86**, 432–440.
- Machado, A. E. H., J. A. de Miranda, R. F. de Freitas, E. T. F. Duarte, L. F. Ferreira, Y. D. Albuquerque, R. Ruggiero, C. Sattler and L. de Oliveira (2003) Destruction of the organic matter present in effluent from a cellulose and paper industry using photocatalysis. *J. Photochem. Photobiol., A* **155**, 231–241.
- Daneshvar, N., M. Ayazloo, A. Khataee and M. Pourhassan (2007) Biological decolorization of dye solution containing Malachite Green by microalgae *Cosmarium* sp. *Bioresour. Technol.* **98**, 1176–1182.
- de Lima, R. O. A., A. P. Bazo, D. M. F. Salvadori, C. M. Rech, D. de Palma Oliveira and G. de Aragão Umbuzeiro (2007) Mutagenic and carcinogenic potential of a textile azo dye processing plant effluent that impacts a drinking water source. *Mutat. Res.* **626**, 53–60.
- Neppolian, B., H. Choi, S. Sakthivel, B. Arabindoo and V. Murugesan (2002) Solar light induced and TiO<sub>2</sub> assisted degradation of textile dye reactive blue 4. *Chemosphere* **46**, 1173–1181.
- Andrade, L. S., L. A. M. Ruotolo, R. C. Rocha-Filho, N. Bocchi, S. R. Biaggio, J. Iniesta, V. García-García and V. Montiel (2007) On the performance of Fe and Fe, F doped Ti–Pt/PbO<sub>2</sub> electrodes in the electrooxidation of the Blue Reactive 19 dye in simulated textile wastewater. *Chemosphere* **66**, 2035–2043.
- Keith, L. H. and D. B. Walters (1991) *National toxicology program's chemical solubility compendium*. CRC Press (Lewis Publishers), Boca Raton, FL.
- Weber, E. J. and V. C. Stickney (1993) Hydrolysis kinetics of reactive blue 19–vinyl sulfone. *Water Res.* **27**, 63–67.
- Özcan, A., Ç. Ömeroğlu, Y. Erdoğan and A. S. Özcan (2007) Modification of bentonite with a cationic surfactant: An adsorption study of textile dye Reactive Blue 19. *J. Hazard. Mater.* **140**, 173–179.
- Asgher, M. and H. N. Bhatti (2012) Removal of reactive blue 19 and reactive blue 49 textile dyes by citrus waste biomass from aqueous solution: Equilibrium and kinetic study. *Canadian J. Chem. Eng.* **90**, 412–419.
- He, Y., G. Li, H. Wang, J. Zhao, H. Su and Q. Huang (2008) Effect of operating conditions on separation performance of reactive dye solution with membrane process. *J. Membr. Sci.* **321**, 183–189.
- Petrinić, I., N. P. R. Andersen, S. Šostar-Turk and A. M. Le Marechal (2007) The removal of reactive dye printing compounds using nanofiltration. *Dyes Pigm.* **74**, 512–518.
- Mahmoodi, V. and J. Sargolzaei (2014) Optimization of photocatalytic degradation of naphthalene using nano-TiO<sub>2</sub>/UV system:

- Statistical analysis by a response surface methodology. *Desalinat. Water Treat.* **52**, 6664–6672.
15. Mahmoodi, V. and J. Sargolzaei (2014) Photocatalytic abatement of naphthalene catalyzed by nanosized TiO<sub>2</sub> particles: Assessment of operational parameters. *Theor. Found. Chem. Eng.* **48**, 656–666.
  16. Mu, R., Z. Xu, L. Li, Y. Shao, H. Wan and S. Zheng (2010) On the photocatalytic properties of elongated TiO<sub>2</sub> nanoparticles for phenol degradation and Cr (VI) reduction. *J. Hazard. Mater.* **176**, 495–502.
  17. Oyama, T., A. Aoshima, S. Horikoshi, H. Hidaka, J. Zhao and N. Serpone (2004) Solar photocatalysis, photodegradation of a commercial detergent in aqueous TiO<sub>2</sub> dispersions under sunlight irradiation. *Sol. Energy* **77**, 525–532.
  18. Gouvea, C. A., F. Wypych, S. G. Moraes, N. Duran, N. Nagata and P. Peralta-Zamora (2000) Semiconductor-assisted photocatalytic degradation of reactive dyes in aqueous solution. *Chemosphere* **40**, 433–440.
  19. Zhang, F., S. Zou, T. Wang, Y. Shi and P. Liu (2017) CeO<sub>2</sub>/Bi<sub>2</sub>WO<sub>6</sub> heterostructured microsphere with excellent visible-light-driven photocatalytic performance for degradation of tetracycline hydrochloride. *Photochem. Photobiol.* <https://doi.org/10.1111/php.12747>.
  20. Chong, M. N., B. Jin, C. W. Chow and C. Saint (2010) Recent developments in photocatalytic water treatment technology: A review. *Water Res.* **44**, 2997–3027.
  21. Pstrowska, K., B. M. Szyja, H. Czapor-Irzabek, A. Kiersnowski and J. Walendziewski (2017) The properties and activity of TiO<sub>2</sub>/beta-SiC nanocomposites in organic dyes photodegradation. *Photochem. Photobiol.* <https://doi.org/10.1111/php.12705>.
  22. Dong, S., Y. Cui, Y. Wang, Y. Li, L. Hu, J. Sun and J. Sun (2014) Designing three-dimensional acicular sheaf shaped BiVO<sub>4</sub>/reduced graphene oxide composites for efficient sunlight-driven photocatalytic degradation of dye wastewater. *Chem. Eng. J.* **249**, 102–110.
  23. Thuillier, G., M. Hersé, D. Labs, T. Foujols, W. Peetermans, D. Gilotay, P. Simon and H. Mandel (2003) The solar spectral irradiance from 200 to 2400 nm as measured by the SOLSPEC spectrometer from the ATLAS and EURECA missions. *Sol. Phys.* **214**, 1–22.
  24. Wang, W., N. Li, Y. Chi, Y. Li, W. Yan, X. Li and C. Shao (2013) Electrospinning of magnetical bismuth ferrite nanofibers with photocatalytic activity. *Ceram. Int.* **39**, 3511–3518.
  25. Chang, X., J. Huang, C. Cheng, Q. Sui, W. Sha, G. Ji, S. Deng and G. Yu (2010) BiOX (X = Cl, Br, I) photocatalysts prepared using NaBiO<sub>3</sub> as the Bi source: Characterization and catalytic performance. *Catal. Commun.* **11**, 460–464.
  26. Ganose, A. M., M. Cuff, K. T. Butler, A. Walsh and D. O. Scanlon (2016) Interplay of orbital and relativistic effects in bismuth oxyhalides: BiOF, BiOCl, BiOBr, and BiOI. *Chem. Mater.* **28**, 1980–1984.
  27. Xiao, X. and W.-D. Zhang (2010) Facile synthesis of nanostructured BiOI microspheres with high visible light-induced photocatalytic activity. *J. Mater. Chem.* **20**, 5866–5870.
  28. Zhang, X., Z. Ai, F. Jia and L. Zhang (2008) Generalized one-pot synthesis, characterization, and photocatalytic activity of hierarchical BiOX (X = Cl, Br, I) nanoplate microspheres. *J. Phys. Chem. C* **112**, 747–753.
  29. Liu, Z., B. Wu, J. Niu, X. Huang and Y. Zhu (2014) Solvothermal synthesis of BiOBr thin film and its photocatalytic performance. *Appl. Surf. Sci.* **288**, 369–372.
  30. Shi, Z.-Q., W. Yan, C.-M. Fan, Y.-F. Wang and G.-Y. Ding (2011) Preparation and photocatalytic activity of BiOCl catalyst. *Trans. Nonferrous Metals Soc. China* **21**, 2254–2258.
  31. Tadjarodi, A., O. Akhavan and K. Bijanzad (2015) Nanosheets of BiOCl incorporated in microflowers: microwave assisted synthesis and dye-photosensitized removal of pollutants. *J. Nanostruct.* **5**, 1–11.
  32. Sharma, I., G. K. Tripathi, V. K. Sharma, S. N. Tripathi, R. Kurchania, C. Kant, A. K. Sharma and K. Saini (2015) One-pot synthesis of three bismuth oxyhalides (BiOCl, BiOBr, BiOI) and their photocatalytic properties in three different exposure conditions. *Cogent Chem.* **1**, 1076371.
  33. Shi, X., X. Chen, X. Chen, S. Zhou and S. Lou (2012) Solvothermal synthesis of BiOI hierarchical spheres with homogeneous sizes and their high photocatalytic performance. *Mater. Lett.* **68**, 296–299.
  34. Taylor, M. G., N. Austin, C. E. Gounaris and G. Mpourmpakis (2015) Catalyst design based on morphology-and environment-dependent adsorption on metal nanoparticles. *ACS Catal.* **5**, 6296–6301.
  35. Ren, K., K. Zhang, J. Liu, H. Luo, Y. Huang and X. Yu (2012) Controllable synthesis of hollow/flower-like BiOI microspheres and highly efficient adsorption and photocatalytic activity. *CrystEngComm* **14**, 4384–4390.
  36. Xia, J., S. Yin, H. Li, H. Xu, Y. Yan and Q. Zhang (2010) Self-assembly and enhanced photocatalytic properties of BiOI hollow microspheres via a reactable ionic liquid. *Langmuir* **27**, 1200–1206.
  37. Song, J. Y. and B. S. Kim (2009) Rapid biological synthesis of silver nanoparticles using plant leaf extracts. *Bioprocess Biosyst. Eng.* **32**, 79.
  38. Malina, D., A. Sobczak-Kupiec, Z. Wzorek and Z. Kowalski (2012) Silver nanoparticles synthesis with different concentrations of polyvinylpyrrolidone. *Dig. J. Nanomater. Bios* **7**, 1527–1534.
  39. Wang, H., X. Qiao, J. Chen, X. Wang and S. Ding (2005) Mechanisms of PVP in the preparation of silver nanoparticles. *Mater. Chem. Phys.* **94**, 449–453.
  40. Zhang, Z., B. Zhao and L. Hu (1996) PVP protective mechanism of ultrafine silver powder synthesized by chemical reduction processes. *J. Solid State Chem.* **121**, 105–110.
  41. Gao, Y., P. Jiang, L. Song, L. Liu, X. Yan, Z. Zhou, D. Liu, J. Wang, H. Yuan and Z. Zhang (2005) Growth mechanism of silver nanowires synthesized by polyvinylpyrrolidone-assisted polyol reduction. *J. Phys. D: Appl. Phys.* **38**, 1061.
  42. Zhang, B. C., H. Y. Yu and D. B. Sun (2010) Shape-controlled synthesis and formation mechanism of cobalt nanopowders by a PVP-assisted method. *Mater. Sci. Forum* **654**, 1186–1189.
  43. Koebel, M. M., L. C. Jones and G. A. Somorjai (2008) Preparation of size-tunable, highly monodisperse PVP-protected Pt-nanoparticles by seed-mediated growth. *J. Nanopart. Res.* **10**, 1063–1069.
  44. Nemamcha, A., H. Moumeni and J. Rehspringer (2009) PVP Protective mechanism of palladium nanoparticles obtained by sonochemical process. *Physics Procedia* **2**, 713–717.
  45. Fanchiang, J.-M. and D.-H. Tseng (2009) Degradation of anthraquinone dye CI Reactive Blue 19 in aqueous solution by ozonation. *Chemosphere* **77**, 214–221.
  46. Rajkumar, D., B. J. Song and J. G. Kim (2007) Electrochemical degradation of Reactive Blue 19 in chloride medium for the treatment of textile dyeing wastewater with identification of intermediate compounds. *Dyes Pigm.* **72**, 1–7.
  47. Lan, Y., B. Mao, E. Wang, Y. Song, Z. Kang, C. Wang, C. Tian, C. Zhang, L. Xu and Z. Li (2007) In-situ fabrication of hybrid polyoxometalate nanoparticles composite films. *Thin Solid Films* **515**, 3397–3401.
  48. Kaur, R. and S. Tripathi (2015) Study of conductivity switching mechanism of CdSe/PVP nanocomposite for memory device application. *Microelectron. Eng.* **133**, 59–65.
  49. Ishikawa, K., K. Yoshikawa and N. Okada (1988) Size effect on the ferroelectric phase transition in PbTiO<sub>3</sub> ultrafine particles. *Phys. Rev. B* **37**, 5852.
  50. Liu, H., W.-R. Cao, Y. Su, Z. Chen and Y. Wang (2013) Bismuth oxyiodide-graphene nanocomposites with high visible light photocatalytic activity. *J. Colloid Interface Sci.* **398**, 161–167.
  51. Zhang, C., H. Zhang, K. Zhang, X. Li, Q. Leng and C. Hu (2014) Photocatalytic activity of ZnWO<sub>4</sub>: Band structure, morphology and surface modification. *ACS Appl. Mater. Interfaces.* **6**, 14423–14432.
  52. Nanda, K. K., F. E. Kruijs and H. Fissan (2001) Energy levels in embedded semiconductor nanoparticles and nanowires. *Nano Lett.* **1**, 605–611.
  53. Deotale, A. J. and R. Nandedkar (2016) Correlation between particle size, strain and band gap of iron oxide nanoparticles. *Mater. Today: Proc.* **3**, 2069–2076.
  54. Nair, S. S., M. Mathews and M. Anantharaman (2005) Evidence for blueshift by weak exciton confinement and tuning of bandgap in superparamagnetic nanocomposites. *Chem. Phys. Lett.* **406**, 398–403.
  55. Kumar, P., H. K. Malik, A. Ghosh, R. Thangavel and K. Asokan (2013) Bandgap tuning in highly c-axis oriented Zn1-xMgxO thin films. *Appl. Phys. Lett.* **102**, 221903.
  56. Zhang, D., X. Yang, X. Hong, Y. Liu and J. Feng (2015) Aluminum nanoparticles enhanced light absorption in silicon solar cell by surface plasmon resonance. *Opt. Quant. Electron.* **47**, 1421–1427.

57. Bastami, T. R. and A. Ahmadpour (2016) Preparation of magnetic photocatalyst nanohybrid decorated by polyoxometalate for the degradation of a pharmaceutical pollutant under solar light. *Environ. Sci. Pollut. Res.* **23**, 8849–8860.
58. Wongkalasin, P., S. Chavadej and T. Sreethawong (2011) Photocatalytic degradation of mixed azo dyes in aqueous wastewater using mesoporous-assembled TiO<sub>2</sub> nanocrystal synthesized by a modified sol–gel process. *Colloids Surf. A* **384**, 519–528.
59. Lovato, M. E., M. L. Fiasconaro and C. A. Martín (2017) Degradation and toxicity depletion of RB19 anthraquinone dye in water by ozone-based technologies. *Water Sci. Technol.* **75**, 813–822.
60. Mera, A. C., D. Contreras, N. Escalona and H. D. Mansilla (2016) BiOI microspheres for photocatalytic degradation of gallic acid. *J. Photochem. Photobiol., A* **318**, 71–76.
61. Rajamanickam, D. and M. Shanthi (2016) Photocatalytic degradation of an organic pollutant by zinc oxide–solar process. *Arab. J. Chem.* **9**, S1858–S1868.
62. Akyol, A., H. Yatmaz and M. Bayramoglu (2004) Photocatalytic decolorization of Remazol Red RR in aqueous ZnO suspensions. *Appl. Catal. B* **54**, 19–24.
63. Behnajady, M., N. Modirshahla and R. Hamzavi (2006) Kinetic study on photocatalytic degradation of CI Acid Yellow 23 by ZnO photocatalyst. *J. Hazard. Mater.* **133**, 226–232.